On the physical limitations for radio frequency absorption in gold nanoparticle suspensions

Sven Nordebo[1], Mariana Dalarsson[1], Yevhen Ivanenko[1], Daniel Sjöberg[2], Richard Bayford[3]

[1] Department of Physics and Electrical Engineering, Linnæus University, 351 95 Växjö, Sweden. E-mail: {sven.nordebo,mariana.dalarsson,yevhen.ivanenko}@lnu.se.
[2] Department of Electrical and Information Technology, Lund University, Box 118, 221 00 Lund, Sweden. E-mail: daniel.sjoberg@eit.lth.se.
[3] The Biophysics and Bioengineering Research Group, Middlesex University, Hendon campus, The Burroughs, London, NW4 4BT, United Kingdom. E-mail: R.Bayford@mdx.ac.uk.

Abstract. This paper presents a study on the physical limitations for radio frequency absorption in gold nanoparticle (GNP) suspensions. A canonical spherical geometry is considered consisting of a spherical suspension of colloidal GNPs characterized as an arbitrary passive dielectric material which is immersed in an arbitrary lossy medium. A relative heating coefficient and a corresponding optimal near field excitation are defined taking the skin effect of the surrounding medium into account. The classical Mie theory for lossy media is also revisited, and it is shown that the optimal permittivity function yielding a maximal absorption inside the spherical suspension is a conjugate match with respect to the surrounding lossy material. A convex optimization approach is used to investigate the broadband realizability of an arbitrary passive material to approximate the desired conjugate match over a finite bandwidth, similar to the approximation of a metamaterial. A narrowband realizability study shows that for a surrounding medium consisting of a weak electrolyte solution, the electromagnetic heating due to the electrophoretic (plasmonic) resonance phenomena inside the spherical GNP suspension can be significant in the microwave regime, provided that the related Drude parameters can be tuned into (or near to) resonance. As a demonstration, some realistic Drude parameters are investigated concerning the volume fraction, mass, and friction constant of the GNPs. The amount of charge that can be accommodated by the GNPs is identified as one of the most important design parameters. However, the problem to reliably model, measure and control the charge number of coated GNPs is not fully understood, and is still an open research issue in this field. The presented theory and related physical limitations provide a useful framework for further research in this direction. Future research is also aiming at an expansion towards arbitrary suspension geometries and the inclusion of thermodynamical analysis.

1. Introduction

A number of publications have proposed that biological tissue can be heated quickly and selectively by the use of gold nanoparticles (GNPs) that are subjected to a strong time-harmonic electromagnetic field, *e.g.*, at 13.56 MHz or in the microwave regime, where the band is chosen due to regulations, see *e.g.*, [1–7]. The aim is to develop a method with the potential to treat cancer. The GNPs can also be used as a contrast agent for electrical impedance tomography, particularly when combined with tumour targeting [8]. The fundamental idea relies on the fact that ligands can be attached to the GNPs to target cancer cells. The rapid rate of growth of the cancer cells causes them to intake an abnormal amount of nutrients and the GNPs can hence be coated with folic acid to target the bio-markers or antigens that are highly specific to the cancer cells, see *e.g.*, [9]. The aim of the radio frequency (RF) or microwave treatment is then to promote local hyperthermia and cell death only in the cancer (cellular necrosis and apoptosis), in addition to increasing the pore size to improve delivery of large-molecule chemotherapeutic and immunotherapeutic agents [7]. The sensitivity of the cancer cells to elevated temperatures enables the tumor growth to be slowed or stopped by transient heating to 40-46 °C for periods of 30 minutes or more, whilst also increasing the tumor sensitivity to chemotherapy and radiotherapy [7, 10]. What is also important is the fact that normal cells typically recover faster than cancer cells when exposed to either heat or the combination of heat and radiation, and hyperthermia does not damage, and may actually enhance, the immune system [7]. Hyperthermia based on targeted heating may therefore be the most potent radio- or chemotherapeutic sensitizer known to date [7, 9, 10].

The physical explanation to the RF-heating of GNPs is not fully understood and there are many phenomenological hypotheses proposed to explain the electromagnetic heating of colloidal gold particles [1–5, 11]. Recently, it has also been questioned whether metal nanoparticles can be heated in radio frequency at all, and several authors have been unable to find neither theoretical nor experimental results to support the hypothesis, see *e.g.*, [1, 12–15]. As *e.g.*, in [15], Mie scattering theory in the Rayleigh limit of small particles is used as an argument to support the (negative) experimental conclusions made in [14].

In this paper, we investigate the physical realizability of achieving a RF-heating in a colloidal GNP suspension, similar as in [2]. However, in the present analysis we are adding the presence of a specific (spherical) structure of the GNP suspension, and investigate the hypothesis that it is the related electrophoretic (plasmonic) resonance phenomena that may cause the heating. To this end, we study the optimal absorption that can be achieved by a physically realizable passive material immersed inside any lossy medium. Previously, optimal absorption has been studied mainly for a lossless exterior domain, such as in [16] giving geometry independent absorption bounds for the plasmonic resonances in metals. In this paper, we prove that the optimal permittivity function yielding a maximal absorption inside a spherical suspension is a conjugate match with respect to the surrounding lossy material. Our formulation also takes the skin effect inside the surrounding lossy

material into account and we show that it is the skin effect that ultimately limits the usefulness of the local heating. The analysis is based on a canonical spherical geometry giving explicit quantitative answers that can be used as an indication towards the physical realizability of the heating. The analysis can also be used as a framework to study and evaluate any particular phenomenological parameter models such as the electrophoretic particle movement which can be described by the Drude model, etc., see *e.g.*, [2, 11]. Numerical examples are included to demonstrate the feasibility of achieving electrophoretic (plasmonic) resonances in the microwave regime in a case when the nanoparticle suspension is immersed in a weak electrolyte solution imitating a typical biological tissue. Here, the frequency band has been chosen around 2.6 GHz constituting a realistic example based on recently proposed hyperthermia measurement devices and nanoparticle setups, see *e.g.*, [6]. It should also be noted that, in practice, the adequate frequency range will be linked to the size and concentration of the nanoparticles, where 5 nm is the maximum size of the GNPs to allow the particles to pass out of the kidney [8]. Realistic Drude parameters are also investigated such as the volume fraction, mass, and friction constant of the GNPs, as described in *e.g.*, [1, 2, 11]. Based on the theoretical framework described above, it is then readily seen that the amount of charge that can be accommodated by the GNPs is one of the most important design parameters in order to achieve a useful resonance and heating. However, even though the net charge of the GNPs has been identified as an important parameter in electrophoretic heating [1, 2, 11], it is presently not well understood how to model, measure or control it, see *e.g.*, [17].

Based on the provided theoretical arguments and numerical examples, we hypothesize that a plausible physical mechanism for achieving an efficient and useful electromagnetic heating of a GNP suspension (structure) is the related electrophoretic (plasmonic) resonance phenomena. We are stressing, however, that further investigations and experiments are needed to support this hypothesis, including in particular the question about GNP net charge, but also thermodynamical considerations such as thermal conductivity and heat transfer, see *e.g.*, [15].

2. Optimal absorption in gold nanoparticle suspensions

2.1. Notation and conventions

The following notation and conventions will be used below. The Maxwell's equations [18] for the electric and magnetic fields $\boldsymbol{E}$ and $\boldsymbol{H}$ are considered based on SI-units and with time convention $\mathrm{e}^{-\mathrm{i}\omega t}$ for time harmonic fields. Let μ_0, ϵ_0, η_0 and c_0 denote the permeability, the permittivity, the wave impedance and the speed of light in vacuum, respectively, and where $\eta_0 = \sqrt{\mu_0/\epsilon_0}$ and $\mathrm{c}_0 = 1/\sqrt{\mu_0\epsilon_0}$. The wavenumber of vacuum is given by $k_0 = \omega\sqrt{\mu_0\epsilon_0}$, where $\omega = 2\pi f$ is the angular frequency and f the frequency. The spherical coordinates are denoted by (r, θ, ϕ), the corresponding unit vectors $(\hat{\boldsymbol{r}}, \hat{\boldsymbol{\theta}}, \hat{\boldsymbol{\phi}})$, and the radius vector $\boldsymbol{r} = r\hat{\boldsymbol{r}}$. The cartesian unit vectors are denoted $(\hat{\boldsymbol{x}}, \hat{\boldsymbol{y}}, \hat{\boldsymbol{z}})$. Finally, the real and imaginary part and the complex conjugate of a complex number ζ are denoted $\Re\{\zeta\}$, $\Im\{\zeta\}$ and ζ^*, respectively.

2.2. Canonical problem setup

A simple canonical problem setup based on spherical geometry is considered as depicted in Figure 1. Here, r_1 is the radius of the spherical suspension of gold nanoparticles and r the radius of a reference surface inside the surrounding medium where the skin effect will be defined. The spherical suspension as well as the surrounding medium are assumed to be non-magnetic, homogeneous and isotropic media with relative permittivity ϵ_1 and ϵ and wavenumbers $k_1 = k_0\sqrt{\epsilon_1}$ and $k = k_0\sqrt{\epsilon}$, respectively.

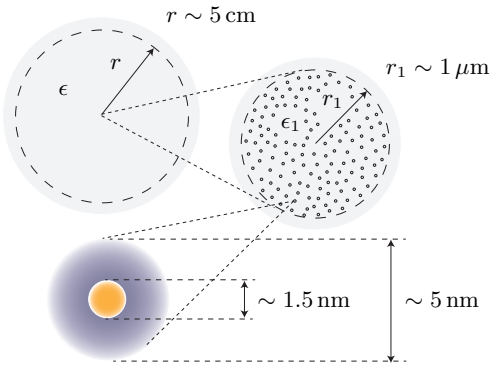

Figure 1. Canonical problem setup based on spherical geometry and related centi-, micro- and nanoscales. The figure also illustrates some typical dimensions for gold nanoparticles coated with glutathione ligands [6, 8].

The following examples of approximative dispersion models will be considered here. The surrounding medium is assumed to consist of a weak electrolyte solution with relative permittivity

$$\epsilon(\omega) = \epsilon_\infty + \frac{\epsilon_\mathrm{s} - \epsilon_\infty}{1 - \mathrm{i}\omega\tau} + \mathrm{i}\frac{\sigma}{\omega\epsilon_0}, \tag{1}$$

where ϵ_∞, ϵ_s and τ are the high frequency permittivity, the static permittivity and the dipole relaxation time in the corresponding Debye model for water, respectively, and σ the conductivity of the saline solution. The suspension of gold nanoparticles is furthermore assumed to consist of a homogeneous

solution of charged nanoparticles where the electric current is governed by an electrophoretic particle acceleration mechanism [1, 2]. Hence, the effective permittivity of the nanoparticle suspension is modeled here as

$$\epsilon_1(\omega) = \epsilon(\omega) + \mathrm{i}\frac{\sigma_1}{\omega\epsilon_0}\frac{1}{1-\mathrm{i}\omega\tau_1}, \tag{2}$$

where σ_1 is the static conductivity and τ_1 the relaxation time in the corresponding Drude model. In an approximate phenomenological description of the electrophoretic mechanism these parameters can be interpreted as $\sigma_1 = \mathcal{N}q^2/\beta$ and $\tau_1 = m/\beta$, where $\mathcal{N}$ is the number of particles per unit volume, q the particle charge, β the friction constant of the host medium and m the particle mass, *cf.*, [2].

2.3. Optimal near field and the skin effect

Consider an expansion of the electromagnetic field in terms of vector spherical waves as outlined in Appendix A.1. It is assumed that all sources are placed outside the surface of radius r as depicted in Figure 1. It is furthermore assumed that the scattering from the nanoparticle suspension is weak and does not interact with any of the possible material obstacles outside the radius r. Hence, the incident and the scattered fields for $r > r_1$ can be represented by regular and outgoing waves with multipole coeffcients $a_{\tau ml}$ and $b_{\tau ml}$, respectively, and the interior field for $r < r_1$ by regular waves with multipole coeffcients $a^{(1)}_{\tau ml}$. The transition matrices give the scattering $b_{\tau ml} = t_{\tau l}a_{\tau ml}$ and the absorption $a^{(1)}_{\tau ml} = r_{\tau l}a_{\tau ml}$, where $t_{\tau l}$ and $r_{\tau l}$ are defined in (A.8) and (A.9) in Appendix A.2.

The mean local heating (in $\mathrm{W/m^3}$) generated inside the nanoparticle suspension of radius r_1 is given by Poynting's theorem as

$$\begin{aligned} P_{\mathrm{loc}}(r_1) &= \frac{3}{4\pi r_1^3}\int_{V_{r_1}} \frac{1}{2}\omega\epsilon_0\Im\{\epsilon_1\}\left|\boldsymbol{E}(\boldsymbol{r})\right|^2 \mathrm{d}v \qquad (3)\\ &= \frac{3\omega\epsilon_0\Im\{\epsilon_1\}}{8\pi r_1^3}\sum_{l=1}^{\infty}\sum_{m=-l}^{l}\sum_{\tau=1}^{2} W_{\tau l}(k_1,r_1)\left|a^{(1)}_{\tau ml}\right|^2\\ &= \frac{3\omega\epsilon_0\Im\{\epsilon_1\}}{8\pi r_1^3}\sum_{l=1}^{\infty}\sum_{m=-l}^{l}\sum_{\tau=1}^{2} W_{\tau l}(k_1,r_1)\left|r_{\tau l}\right|^2\left|a_{\tau ml}\right|^2, \end{aligned}$$

where the orthogonality of the regular vector spherical waves $\mathbf{v}_{\tau ml}(k_1\boldsymbol{r})$ have been used, V_{r_1} denotes the spherical volume of radius r_1 and where $W_{\tau l}(k_1,r_1) = \int_{V_{r_1}}\left|\mathbf{v}_{\tau ml}(k_1\boldsymbol{r})\right|^2\mathrm{d}v$, *cf.*, (A.18) and (A.19). In (3), the relation $a^{(1)}_{\tau ml} = r_{\tau l}a_{\tau ml}$ has also been inserted. It is shown in Appendix A.3 and Appendix A.4 that

$$W_{1l}(k_1,r_1) = \frac{r_1^2\Im\{k_1\mathrm{j}_{l+1}(k_1r_1)\mathrm{j}_l^*(k_1r_1)\}}{\Im\{k_1^2\}}, \tag{4}$$

$$\begin{aligned} W_{2l}(k_1,r_1) = \frac{1}{2l+1}\big((l+1)W_{1,l-1}(k_1,r_1) \qquad (5)\\ +lW_{1,l+1}(k_1,r_1)\big), \end{aligned}$$

where $\mathrm{j}_l(\cdot)$ are the spherical Bessel functions of order l, *cf.*, (A.19), (A.20) and (A.21).

As a quantitative measure of the skin effect, the mean background heating (in $\mathrm{W/m^3}$) at radius r in the surrounding medium is defined by

$$\begin{aligned} P_{\mathrm{b}}(r) &= \frac{1}{4\pi r^2}\int_{S_r}\frac{1}{2}\omega\epsilon_0\Im\{\epsilon\}\left|\boldsymbol{E}(\boldsymbol{r})\right|^2\mathrm{d}S \qquad (6)\\ &= \frac{1}{8\pi}\omega\epsilon_0\Im\{\epsilon\}\int_{\Omega_0}\left|\boldsymbol{E}(\boldsymbol{r})\right|^2\mathrm{d}\Omega, \qquad (7) \end{aligned}$$

where S_r denotes the spherical boundary of radius r, Ω_0 the unit sphere and $\mathrm{d}S = r^2\mathrm{d}\Omega$ with $\mathrm{d}\Omega$ the differential solid angle. By exploiting the orthogonality of the vector spherical waves (A.16), the mean background loss can now be expressed as

$$P_{\mathrm{b}}(r) = \frac{1}{8\pi}\omega\epsilon_0\Im\{\epsilon\}\sum_{l=1}^{\infty}\sum_{m=-l}^{l}\sum_{\tau=1}^{2} S_{\tau l}(k,r)\left|a_{\tau ml}\right|^2, \tag{8}$$

where $S_{\tau l}(k,r) = \int_{\Omega_0}\left|\mathbf{v}_{\tau ml}(k\boldsymbol{r})\right|^2\mathrm{d}\Omega$, see also (A.17).

The optimal near field is now defined by the maximization of the relative heating coefficient $F = P_{\mathrm{loc}}(r_1)/P_{\mathrm{b}}(r)$ at some radius r. This power ratio is a generalized Rayleigh quotient and hence the problem is equivalent to finding the maximum eigenvalue in the corresponding (diagonal) generalized eigenvalue problem as follows

$$\max_{|a_{\tau ml}|^2}\frac{P_{\mathrm{loc}}(r_1)}{P_{\mathrm{b}}(r)} = \frac{3}{r_1^3}\frac{\Im\{\epsilon_1\}}{\Im\{\epsilon\}}\max_{\tau,l}\frac{W_{\tau l}(k_1,r_1)\left|r_{\tau l}\right|^2}{S_{\tau l}(k,r)}. \tag{9}$$

With the relatively low frequencies and small geometrical dimensions of interest in this paper, the optimal near field excitation is generally obtained with an electric dipole field ($\tau = 2$ and $l = 1$ in (9)) yielding the relative heating coefficient

$$F(\epsilon_1) = \frac{3}{r_1^3}\frac{\Im\{\epsilon_1\}}{\Im\{\epsilon\}}\frac{W_{21}(k_1,r_1)\left|r_{21}\right|^2}{S_{21}(k,r)}, \tag{10}$$

where $F(\epsilon_1)$ is considered to be a function of the complex-valued permittivity ϵ_1 (or frequency ω) when all other parameters are fixed.

2.4. Asymptotic analysis

Based on the asymptotic expansions of the spherical Bessel and Hankel functions for small arguments [19] $\mathrm{j}_0(x) \sim 1$, $\mathrm{j}_1(x) \sim \frac{1}{3}x$, $\mathrm{j}_1'(x) \sim \frac{1}{3}$, $\mathrm{j}_2(x) \sim \frac{1}{15}x^2$, $\mathrm{j}_3(x) \sim \frac{1}{105}x^3$, $\mathrm{h}_1^{(1)}(x) \sim -\frac{\mathrm{i}}{x^2}$ and $\mathrm{h}_1^{(1)\prime}(x) \sim \frac{2\mathrm{i}}{x^3}$, it is found that

$$W_{21} \sim \frac{2}{9}r_1^3, \tag{11}$$

$$r_{21} \sim \frac{3\epsilon}{\epsilon_1+2\epsilon}, \tag{12}$$

in the asymptotic limit of small r_1. Hence, for small r_1 the asymptotic relative heating coefficient can be expressed as

$$F^{\mathrm{a}}(\epsilon_1) = \frac{F^{\mathrm{a}}_{\mathrm{num}}(\epsilon_1)}{S_{21}(k,r)}, \tag{13}$$

where the numerator is given by

$$F^{\mathrm{a}}_{\mathrm{num}}(\epsilon_1) = 6\frac{|\epsilon|^2}{\Im\{\epsilon\}}\frac{\Im\{\epsilon_1\}}{|\epsilon_1 - \epsilon^*_{1\mathrm{o}}|^2}, \tag{14}$$

and where the quantity $\epsilon_{1\mathrm{o}}$ is defined by $\epsilon^*_{1\mathrm{o}} = -2\epsilon$. Note that $F^{\mathrm{a}}(\epsilon_1)$ is independent of the radius r_1.

2.5. Optimal absorption and the conjugate match

Although it is not easy to prove in general that $F(\epsilon_1)$ defined in (10) is a convex function of ϵ_1 for $\Im\epsilon_1 > 0$, it is straightforward to show that $\epsilon_{1\mathrm{o}} = -2\epsilon^*$ is a local maximum of $F^{\mathrm{a}}_{\mathrm{num}}(\epsilon_1)$ defined in (14). Hence, let $F_0(\epsilon_1, \epsilon^*_1) = \frac{\Im\epsilon_1}{|\epsilon_1 - \epsilon^*_{1\mathrm{o}}|^2}$ and consider the following Taylor expansion in a neighbourhood of $\epsilon_{1\mathrm{o}}$

$$\begin{aligned} F_0(\epsilon_1, \epsilon^*_1) &= -\mathrm{i}\frac{\epsilon_1 - \epsilon^*_1}{2}\frac{1}{\epsilon_1 - \epsilon^*_{1\mathrm{o}}}\frac{1}{\epsilon^*_1 - \epsilon_{1\mathrm{o}}} \\ &= F_0(\epsilon_{1\mathrm{o}}, \epsilon^*_{1\mathrm{o}}) + \frac{\partial F_0}{\partial \epsilon_1}(\epsilon_1 - \epsilon_{1\mathrm{o}}) + \frac{\partial F_0}{\partial \epsilon^*_1}(\epsilon^*_1 - \epsilon^*_{1\mathrm{o}}) \\ &+ \frac{1}{2}\frac{\partial^2 F_0}{\partial \epsilon_1^2}(\epsilon_1 - \epsilon_{1\mathrm{o}})^2 + \frac{1}{2}\frac{\partial^2 F_0}{\partial \epsilon_1^{*2}}(\epsilon^*_1 - \epsilon^*_{1\mathrm{o}})^2 \\ &+ \frac{\partial^2 F_0}{\partial \epsilon_1 \partial \epsilon^*_1}(\epsilon_1 - \epsilon_{1\mathrm{o}})(\epsilon^*_1 - \epsilon^*_{1\mathrm{o}}) + \cdots, \end{aligned} \tag{15}$$

where the complex derivatives $\frac{\partial}{\partial \epsilon_1}$ and $\frac{\partial}{\partial \epsilon^*_1}$ are defined as in [20]. It is straightforward to show that

$$\frac{\partial F_0}{\partial \epsilon_1} = \frac{\partial F_0}{\partial \epsilon^*_1} = \frac{\partial^2 F_0}{\partial \epsilon_1^2} = \frac{\partial^2 F_0}{\partial \epsilon_1^{*2}} = 0 \tag{16}$$

at $\epsilon_1 = \epsilon_{1\mathrm{o}}$ and

$$\frac{\partial^2 F_0}{\partial \epsilon_1 \partial \epsilon^*_1} = -\frac{\Im\{\epsilon_{1\mathrm{o}}\}}{|\epsilon_1 - \epsilon^*_{1\mathrm{o}}|^4}, \tag{17}$$

which is negative definite when $\Im\{\epsilon_{1\mathrm{o}}\} > 0$. It is noted that the passivity of the external material with $\Im\{\epsilon\} > 0$ guarantees that $\epsilon_{1\mathrm{o}} = -2\epsilon^*$ has a positive imaginary part. Hence, the conjugate match‡ $\epsilon_{1\mathrm{o}} = -2\epsilon^*$ yields a maximum of the relative heating function $F^{\mathrm{a}}(\epsilon_1)$ in (13) and an optimal absorption inside the suspension domain with radius r_1.

2.6. Relation to general Mie theory

The expression for the absorption cross section C_{abs} of a small homogeneous dielectric sphere in a lossy medium is obtained from general Mie theory as

$$C_{\mathrm{abs}} = C_{\mathrm{inc}} - C_{\mathrm{sca}} + C_{\mathrm{ext}}, \tag{18}$$

‡ Note that the factor 2 in $\epsilon_{1\mathrm{o}} = -2\epsilon^*$ is a form factor associated with the spherical geometry, see for instance [19, p. 145].

where the scattering cross section C_{sca}, the extinction cross section C_{ext} and the compensation term C_{inc} (power absorbed from the incident plane wave in the surrounding medium) are given by

$$C_{\mathrm{sca}} = \frac{16\pi}{3}k_0 r_1^3 \Im\{\sqrt{\epsilon}\}\left|\frac{\epsilon_1 - \epsilon}{\epsilon_1 + 2\epsilon}\right|^2, \tag{19}$$

$$\begin{aligned} C_{\mathrm{ext}} &= 6\pi k_0 r_1^3 \left[\frac{4}{9}\Re\left\{\frac{\epsilon_1 - \epsilon}{\epsilon_1 + 2\epsilon}\right\}\Im\{\sqrt{\epsilon}\}\right. \\ &\left. + \frac{2}{3}\Im\left\{\frac{\epsilon_1 - \epsilon}{\epsilon_1 + 2\epsilon}\right\}\left(\Re\{\sqrt{\epsilon}\} - \frac{(\Im\{\sqrt{\epsilon}\})^2}{\Re\{\sqrt{\epsilon}\}}\right)\right], \end{aligned} \tag{20}$$

$$C_{\mathrm{inc}} = \frac{8\pi}{3}k_0 r_1^3 \Im\{\sqrt{\epsilon}\}, \tag{21}$$

see *e.g.*, [2, 21–23]. By algebraic manipulation of (18) through (21) (or by performing the derivation from first principles), it can be shown that the absorption cross section is given by

$$C_{\mathrm{abs}} = 12\pi k_0 r_1^3 \frac{|\epsilon|^2}{\Re\{\sqrt{\epsilon}\}}\frac{\Im\{\epsilon_1\}}{|\epsilon_1 + 2\epsilon|^2}, \tag{22}$$

which has a striking resemblance to the heating coefficent given by (14). Hence, the resulting expression (22) immediately verifies that the conjugate match $\epsilon_{1\mathrm{o}} = -2\epsilon^*$ is also optimal with respect to the absorption cross section associated with a small dielectric sphere in a lossy medium in accordance with the Mie theory.

2.7. Narrowband realizability of the conjugate match: Tuning the Drude model

Now that we have shown that the conjugate match $\epsilon_{1\mathrm{o}} = -2\epsilon^*$ yields the optimal absorption at any given frequency ω, the next step is to consider the realizability of an interior permittivity function $\epsilon_1(\omega)$ that can achieve this property. With a "normal" surrounding medium having a permittivity function ϵ with $\Re\{\epsilon\} > 0$, this requires a permittivity function for the interior region with a negative real part $\Re\{\epsilon_1\} < 0$, a material property that sometimes is associated with a *metamaterial* and which may have severe limitations on the bandwidth capabilities, *cf.*, [24].

Given that the approximate electrophoretic particle acceleration mechanism described above is valid, it is straightforward to "tune" the corresponding Drude model in (2) to resonance at the desired frequency ω_{d} by solving the equation

$$\epsilon_1(\omega_{\mathrm{d}}) = \epsilon(\omega_{\mathrm{d}}) + \mathrm{i}\frac{\sigma_1}{\omega_{\mathrm{d}}\epsilon_0}\frac{1}{1 - \mathrm{i}\omega_{\mathrm{d}}\tau_1} = \epsilon_{1\mathrm{o}}(\omega_{\mathrm{d}}), \tag{23}$$

yielding the following tuned parameters

$$\tau_1 = \frac{1}{\omega_{\mathrm{d}}}\frac{\Re\epsilon(\omega_{\mathrm{d}}) - \Re\epsilon_{1\mathrm{o}}(\omega_{\mathrm{d}})}{\Im\epsilon_{1\mathrm{o}}(\omega_{\mathrm{d}}) - \Im\epsilon(\omega_{\mathrm{d}})}, \tag{24}$$

$$\sigma_1 = \epsilon_0\left(\Re\epsilon(\omega_{\mathrm{d}}) - \Re\epsilon_{1\mathrm{o}}(\omega_{\mathrm{d}})\right)\frac{1 + \omega_{\mathrm{d}}^2\tau_1^2}{\tau_1}. \tag{25}$$

It should be noted that the inclusion of the term $\epsilon(\omega)$ in (2) and (23) above is "ad hoc", and can be replaced for any other model as long as the term $\Im\epsilon_{1\mathrm{o}}(\omega_\mathrm{d}) - \Im\epsilon(\omega_\mathrm{d}) > 0$ in (24) above.

2.8. Broadband realizability of the conjugate match: Optimal dispersion modeling

To study the optimal capabilities of a passive material with permittivity $\epsilon_1(\omega)$ to approximate the desired conjugate match $\epsilon_{1\mathrm{o}}(\omega) = -2\epsilon^*(\omega)$ over a given bandwidth, a convex optimization approach is employed as follows, see also [25]. The permittivity function of any passive material $\epsilon_1(\omega)$ corresponds to a symmetric Herglotz function $h_1(\omega) = \omega\epsilon_1(\omega)$, where $\omega \in \mathbb{C}_+ = \{\omega \in \mathbb{C} | \Im\omega > 0\}$, see *e.g.*, [24, 26–30]. Symmetric Herglotz functions are analytic functions with symmetry $h_1(\omega) = -h_1^*(-\omega^*)$ mapping the upper half-plane into itself and which allow for an integral representation based on positive measures. On the real line this integral representation becomes a Cauchy-principal value integral (Hilbert transform) acting on the regular part of the measure plus the contribution from possible point masses. Here, the limiting Herglotz function for $\omega \in \mathbb{R}$ is represented by

$$h_1(\omega) = \omega\epsilon_{1\infty} + \frac{1}{\pi}\int_{-\infty}^{\infty} \frac{1}{\xi - \omega}\Im h_{1\mathrm{r}}(\xi)\mathrm{d}\xi + x_0\frac{1}{-\omega} + \mathrm{i}\left(\Im h_{1\mathrm{r}}(\omega) + \pi x_0\delta(\omega)\right), \tag{26}$$

where $\epsilon_{1\infty}$ is the high frequency permittivity, $\Im h_{1\mathrm{r}}(\xi)$ the regular part of the positive symmetric measure and where a point mass with amplitude $x_0 \geq 0$ at $\omega = 0$ has been included. Obviously, the point mass at $\omega = 0$ will be very efficient in generating a negative real part of $h_1(\omega)$ at any particular desired frequency ω_d.

Next, a finite optimization domain Ω_r (support of the regular measure) is defined with $0 \notin \Omega_\mathrm{r}$ and where the positive symmetric measure is approximated by using

$$\Im h_{1\mathrm{r}}(\omega) = \sum_{n=1}^{N} x_n \left[p_n(\omega) + p_n(-\omega)\right], \tag{27}$$

where $p_n(\omega)$ are triangular basis functions defined on Ω_r and $x_n \geq 0$ the corresponding optimization variables for $n = 1, \ldots, N$. Further, a finite approximation domain $\Omega \subset \Omega_\mathrm{r}$ is defined and the corresponding real part $\Re h_{1\mathrm{r}}(\omega)$ on Ω is given by

$$\Re h_{1\mathrm{r}}(\omega) = \sum_{n=1}^{N} x_n \left[\hat{p}_n(\omega) - \hat{p}_n(-\omega)\right], \tag{28}$$

where $\hat{p}_n(\omega) = \frac{1}{\pi}\int_{-\infty}^{\infty} \frac{1}{\xi - \omega} p_n(\xi)\mathrm{d}\xi$ is the (negative) Hilbert transform of the triangular pulse function $p_n(\omega)$, *cf.*, [31]. The discrete representation (26) through (28) can now be used to formulate the following convex optimization problem

$$\begin{array}{ll} \text{minimize} & \|h_1(\omega) - f(\omega)\|_\Omega \\ \text{subject to} & x_n \geq 0, \\ & \epsilon_{1\infty} \geq 1, \end{array} \tag{29}$$

where the target function is $f(\omega) = \omega\epsilon_{1\mathrm{o}}(\omega)$ and $\|\cdot\|_\Omega$ a suitable norm defined on Ω, see also [25]. Here, x_n with $n = 0, 1, \ldots, N$ and $\epsilon_{1\infty}$ are the positive optimization variables. The optimization problem (29) can be solved efficiently using the CVX Matlab software for disciplined convex programming [32]. Typically, Ω consists of a set of frequency points sampled around the desired center frequency ω_d. If ω_d is large (such as in the GHz range), it is usually necessary to employ scaled dimensionless variables x_n/ω_d for $n = 1, \ldots, N$ and x_0/ω_d^2 to maintain numerical stability.

3. Numerical examples

To illustrate the theory above the following numerical example is considered. The surrounding medium is assumed to consist of a weak electrolyte solution with relative permittivity given by (1) and where $\epsilon_\infty = 5.27$, $\epsilon_\mathrm{s} = 80$ and $\tau = 10^{-11}\,\mathrm{s}$ are the Debye parameters for water and $\sigma \in \{0.1, 1, 10\}\,\mathrm{S/m}$ the conductivity parameters of the saline solution. The radii of the reference surface and the spherical suspension are $r = 5\,\mathrm{cm}$ and $r_1 = 1\,\mu\mathrm{m}$, respectively. In all of the numerical results below, the optimality of using electric dipole excitation ($\tau = 2$, $l = 1$) has been verified by evaluating (9) with $\tau = 1, 2$ and $l = 1, 2, 3, \ldots$, etc.

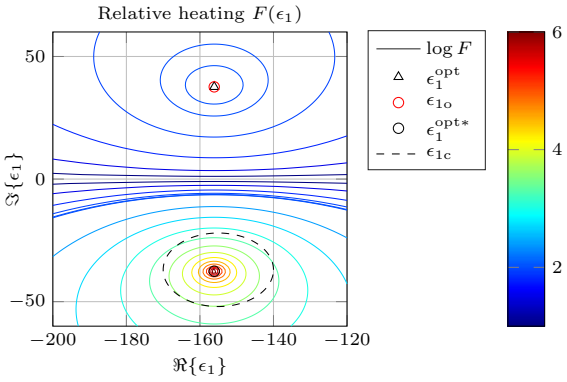

Figure 2. Contour plot of the relative heating $F(\epsilon_1)$ as a function of the complex permitivity ϵ_1 at frequency $f_\mathrm{d} = 2.6\,\mathrm{GHz}$. The surrounding medium is a saline solution with conductivity $\sigma = 1\,\mathrm{S/m}$.

In Figure 2 is shown a contour plot of the relative heating coefficient $F(\epsilon_1)$ given by the rigorous expression (10). The surrounding medium is a saline solution with conductivity $\sigma = 1\,\mathrm{S/m}$ and the desired center frequency is $f_\mathrm{d} = 2.6\,\mathrm{GHz}$. The plot clearly illustrates the concavity of the target function $F(\epsilon_1)$ in

the upper half-plane $\Im\epsilon_1 > 0$. Here, $\epsilon_1^{\text{opt}*}$ is obtained from a numerical residue calculation in the lower half-plane as $\epsilon_1^{\text{opt}*} = (\oint_{\epsilon_{1c}} a^{-1}(\epsilon_1)\epsilon_1 \mathrm{d}\epsilon_1)/(\oint_{\epsilon_{1c}} a^{-1}(\epsilon_1)\mathrm{d}\epsilon_1)$, where $a(\epsilon_1)$ is the analytic denominator (determinant) associated with r_{21} defined in (A.9) and ϵ_{1c} an arbitrary contour circumscribing the pole (zero) location of r_{21} ($a(\epsilon_1)$). Further, ϵ_{1o} denotes the conjugate match $\epsilon_{1o} = -2\epsilon^*$ which is the asymptotic solution that yields a maximal absorption for small r_1. In this numerical example $\epsilon_1^{\text{opt}} = -156.12 + \mathrm{i}37.609$ and $\epsilon_{1o} = -156.11 + \mathrm{i}37.609$, demonstrating the high accuracy of the asymptotic solution.

3.1. Tuning the Drude model

In Figure 3 is shown the constituents of $F^{\text{a}} = F^{\text{a}}_{\text{num}}/S_{21}$ given by (13) and (14) plotted as functions of frequency and where $\epsilon_1(\omega)$ is given by the Drude model (2) tuned to resonance at $f_{\text{d}} = 2.6\,\text{GHz}$ by using (24) and (25). Here, $\sigma = 0.1\,\text{S/m}$ and the maximum relative heating is $F^{\text{a}} = 1614$ close to the center frequency at $f_{\text{d}} = 2.6\,\text{GHz}$.

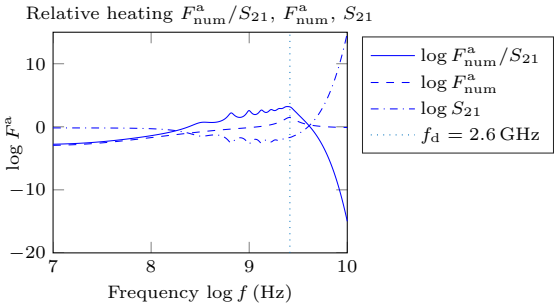

Figure 3. Relative heating $F^{\text{a}} = F^{\text{a}}_{\text{num}}/S_{21}$ and its constituents $F^{\text{a}}_{\text{num}}$ and S_{21} plotted as functions of frequency. Here, $\epsilon_1(\omega)$ is given by the Drude model tuned to resonance at $f_{\text{d}} = 2.6\,\text{GHz}$ and the surrounding medium is a saline solution with conductivity $\sigma = 0.1\,\text{S/m}$.

The oscillations seen at lower frequencies are merely "resonances" associated with the reference surface at $r = 5\,\text{cm}$ and are visible also in the function S_{21}. The increase in S_{21} at higher frequencies is a manifestation of the skin effect in the surrounding medium which will ultimately limit the potential of relative heating.

In Figures 4 and 5 are shown the corresponding optimal relative heating F^{a} and numerator $F^{\text{a}}_{\text{num}}$ for $\sigma \in \{0.1, 1, 10\}\,\text{S/m}$. The corresponding optimally tuned Drude parameters are $\tau_1 \in \{11.4, 7.6, 1.8\}\cdot 10^{-10}\,\text{s}$ and $\sigma_1 \in \{632, 425, 110\}\,\text{S/m}$. The corresponding maximal relative heating at $f_{\text{d}} = 2.6\,\text{GHz}$ is obtained as $F^{\text{a}} \in \{1614, 126, 10^{-6}\}$ illustrating in this example a great potential of local heating when $\sigma \in \{0.1, 1\}\,\text{S/m}$. However, the result for $\sigma = 10\,\text{S/m}$ implies that the surrounding medium is too lossy and the resulting skin effect will render the local heating useless.

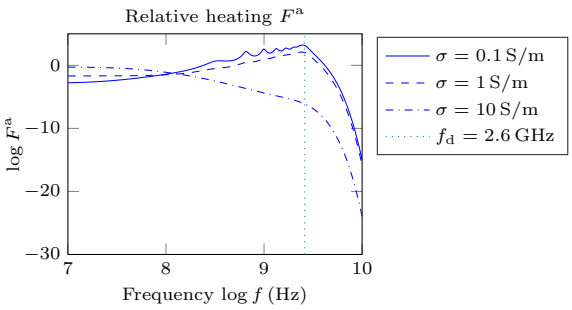

Figure 4. Relative heating F^{a} as a function of frequency. Here, $\epsilon_1(\omega)$ is given by the Drude model tuned to resonance at $f_{\text{d}} = 2.6\,\text{GHz}$ and the surrounding medium is a saline solution with conductivity $\sigma \in \{0.1, 1, 10\}\,\text{S/m}$.

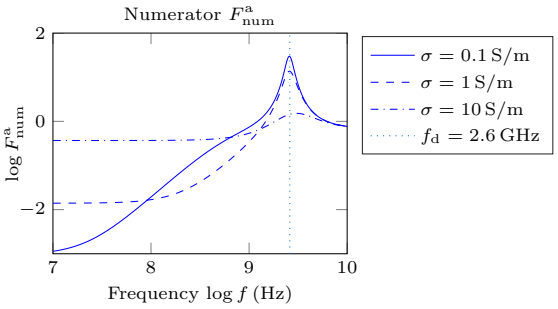

Figure 5. Numerator $F^{\text{a}}_{\text{num}}$ as a function of frequency. Here, $\epsilon_1(\omega)$ is given by the Drude model tuned to resonance at $f_{\text{d}} = 2.6\,\text{GHz}$ and the surrounding medium is a saline solution with conductivity $\sigma \in \{0.1, 1, 10\}\,\text{S/m}$.

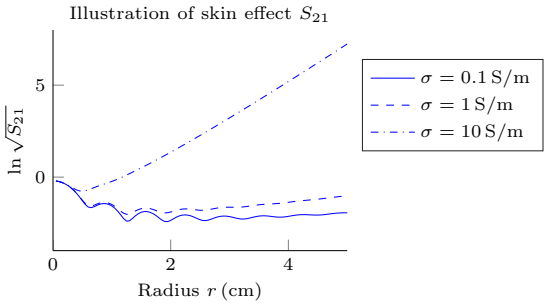

Figure 6. Illustration of the skin effect with $\ln\sqrt{S_{21}}$ plotted as a function of radius r at $f_{\text{d}} = 2.6\,\text{GHz}$ and where $\sigma \in \{0.1, 1, 10\}\,\text{S/m}$.

The skin effect is further illustrated in Figure 6 with $\ln\sqrt{S_{21}}$ plotted as a function of radius r at $f_{\text{d}} = 2.6\,\text{GHz}$ and where $\sigma \in \{0.1, 1, 10\}\,\text{S/m}$. The skin depth can be interpreted here as the radial distance through which the amplitude $\sqrt{S_{21}}$ has decreased by a factor of e^{-1}. Hence, the skin depth in the example case with $\sigma = 10\,\text{S/m}$ is seen to be less than 1 cm.

3.2. Parameter studies

A simple parameter study is presented below to

illustrate how the derived optimal bound and the tuned Drude model can be employed in a comparison and an evaluation of some realistic parameter choices regarding the electrophoretic particle acceleration mechanism as described in [1, 2]. Here, the surrounding medium is assumed to have a permittivity ϵ given by (1) with salinity $\sigma = 0.1\,\mathrm{S/m}$ and all other Debye parameters fixed as above. The spherical suspension of GNPs has a radius $r_1 = 1\,\mu\mathrm{m}$ with permittivity ϵ_1 and the optimal conjugate match is given by $\epsilon_{1o} = -2\epsilon^*$. The tuned Drude model ϵ_{1D} is defined by (24) and (25) and is tuned to resonance at $f_\mathrm{d} = 2.6\,\mathrm{GHz}$.

The theoretical bounds and the hypothetical tuned Drude model defined above are now compared to a realistic Drude model (2) where the GNPs consist of a gold core coated with a shell of electrically charged ligands. The radius of the GNP with ligands is $a = 2.5\,\mathrm{nm}$ and the radius of the gold core is $a_\mathrm{Au} = 0.75\,\mathrm{nm}$, *cf.*, Figure 1. The mass of the GNP is $m = ((4\pi a_\mathrm{Au}^3)/3)\rho_\mathrm{Au} + ((4\pi a^3)/3 - (4\pi a_\mathrm{Au}^3)/3)\rho_L$ where $\rho_{Au} = 19300\,\mathrm{kg/m^3}$ and $\rho_L = 1000\,\mathrm{kg/m^3}$ are the assumed mass densities of gold and ligands, respectively. The net charge of the GNP is modeled as $q = (3a_\mathrm{Au} + 0.5a_\mathrm{Au}^2)e_0 + n_\mathrm{L}e_0$ where the charge of the gold core is modeled as in [2], n_L is the assumed net electron count in the ligand shell and e_0 denotes the electron charge $e_0 = 1.6{\cdot}10^{-19}\,\mathrm{C}$. The friction constant β is modelled as $\beta = 6\pi\mu_\mathrm{f}a$ where $\mu_\mathrm{f} = 10^{-3}\,\mathrm{Nsm^{-2}}$ is the dynamic shear viscosity of the host medium (water at room temperature) as in [2]. Let ϕ denote the volume fraction of GNPs in the spherical suspension. The number of particles per unit volume is then given by $\mathcal{N} = \phi/(4\pi a^3/3)$. In the numerical example below, we have chosen $\phi = 2\cdot 10^{-3}$ as in [2]. Now, the corresponding parameters of a realistic Drude model can be calculated as $\sigma_1 = \mathcal{N}q^2/\beta$ and $\tau_1 = m/\beta$.

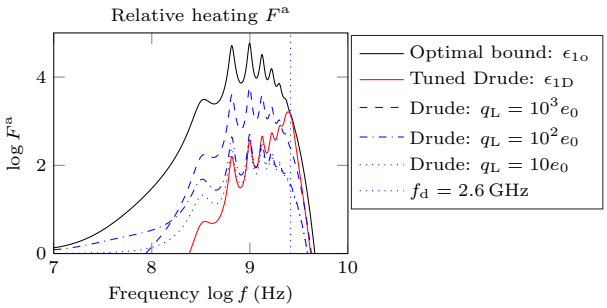

Figure 7. Relative heating F^a as a function of frequency. Here, the optimal bound corresponds to the conjugate match $\epsilon_{1o}(\omega)$, $\epsilon_{1D}(\omega)$ the Drude model tuned to resonance at $f_\mathrm{d} = 2.6\,\mathrm{GHz}$, and finally three realistic cases of Drude models where $q_\mathrm{L} \in \{10, 10^2, 10^3\}e_0$ are the corresponding charges of the GNP ligands. The radius of the spherical suspension is $r_1 = 1\,\mu\mathrm{m}$ and the surrounding medium is a saline solution with conductivity $\sigma = 0.1\,\mathrm{S/m}$.

In Figure 7 and Figure 8 are shown the relative heating F^a given by (13), and the absorption cross section C_abs given by (22), respectively, in a comparison based on the optimal, the tuned and the realistic Drude parameter models as explained above. In this numerical study we found that the resulting heating curves did not change notably when imposing significant changes in the volume fraction ϕ, the ligand mass density ρ_L nor in the viscosity parameter μ_f above. With the present parameter setting the most sensitive parameter issue appeared to be the necessity of having a sufficiently large net charge of ligands, $q_\mathrm{L} = n_\mathrm{L}e_0$, to get significant heating. For this reason, we have plotted in Figure 7 and Figure 8 the heating corresponding to the realistic Drude models based on ligand charges with $q_\mathrm{L} \in \{10, 10^2, 10^3\}e_0$. Since the ratio between the local heating and the skin heating, F^a, in these examples are in the order of 100 to 1000, it is concluded that the potential of electromagnetic heating of a GNP suspension based on electrophoretic resonances in the microwave regime is very promising and is a topic that should be investigated further.

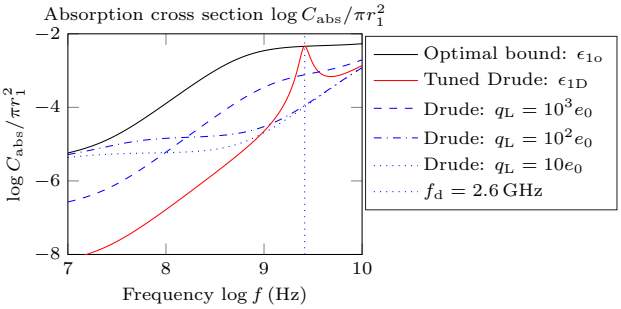

Figure 8. Absorption cross section C_abs as a function of frequency. Here, the optimal bound corresponds to the conjugate match $\epsilon_{1o}(\omega)$, $\epsilon_{1D}(\omega)$ the Drude model tuned to resonance at $f_\mathrm{d} = 2.6\,\mathrm{GHz}$, and finally three realistic cases of Drude models where $q_\mathrm{L} \in \{10, 10^2, 10^3\}e_0$ are the corresponding charges of the GNP ligands. The radius of the spherical suspension is $r_1 = 1\,\mu\mathrm{m}$ and the surrounding medium is a saline solution with conductivity $\sigma = 0.1\,\mathrm{S/m}$.

3.3. Optimal dispersion modeling

The convex optimization formulation (29) is employed here to study the optimal capabilities of a passive material with permittivity $\epsilon_1(\omega)$ to approximate the desired conjugate match $\epsilon_{1o}(\omega)$ over a given bandwidth. The norm is defined by $\|h_1(\omega) - f(\omega)\|_\Omega = \sup_\Omega |(h_1(\omega) - f(\omega))/\omega| = \sup_\Omega |\epsilon_1(\omega) - \epsilon_{1o}(\omega)|$. Here, the target function is the conjugate match $\epsilon_{1o}(\omega) = -2\epsilon^*(\omega)$, where $\epsilon(\omega)$ is the permittivity function of the surrounding medium given by (1) with Debye parameters $\epsilon_\infty = 5.27$, $\epsilon_\mathrm{s} = 80$ and $\tau = 10^{-11}\,\mathrm{s}$ as above and $\sigma = 1\,\mathrm{S/m}$. The optimization domain for dispersion modeling (support of the regular measure) is $\Omega_\mathrm{r} = [2.4, 2.8]\,\mathrm{GHz}$ with $N = 300$ triangular basis

functions and corresponding optimization variables x_n for $n = 1, \ldots, N$. Further optimization variables are the high frequency permittivity $\epsilon_{1\infty}$ and the amplitude x_0 of the point mass at $\omega = 0$. The finite approximation domain Ω (support of the norm) is defined by the nodal points of the approximating triangular basis functions sampled in the interval $[2.5, 2.7]$ GHz, which is centered at the desired frequency $f_\mathrm{d} = 2.6$ GHz.

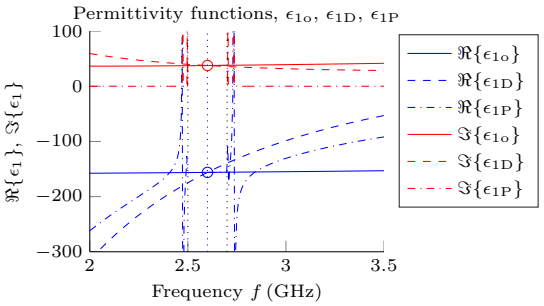

Figure 9. Permittivity functions corresponding to the target conjugate match $\epsilon_{1\mathrm{o}}$, the tuned Drude model $\epsilon_{1\mathrm{D}}$ and the optimized passive model $\epsilon_{1\mathrm{P}}$. The surrounding medium is a saline solution with conductivity $\sigma = 1$ S/m and the approximation domain is $\Omega = [2.5, 2.7]$ GHz.

In Figure 9 is shown the target permittivity $\epsilon_{1\mathrm{o}}(\omega)$, the tuned Drude model $\epsilon_{1\mathrm{D}}(\omega)$ according to section 3.1 above and the resulting optimum passive (realizable) model $\epsilon_{1\mathrm{P}}(\omega)$, plotted as functions of frequency between 2 and 3.5 GHz. The optimized model $\epsilon_{1\mathrm{P}}(\omega)$ consists of a high frequency permittivity $\epsilon_{1\infty} = 1$, a point mass at $\omega = 0$ with amplitude $x_0 = 160.5\omega_\mathrm{d}^2$ and a regular measure $\Im h_{1\mathrm{r}}(\omega)$ yielding an impulsive response just outside and close to the approximation domain and finally a response that closely matches the target permittivity $\epsilon_{1\mathrm{o}}(\omega)$ inside the approximation domain. Except for the support of these responses, $\Im h_{1\mathrm{r}}(\omega)$ is essentially zero elsewhere and the solution is hence independent of an increase of the optimization domain Ω_r.

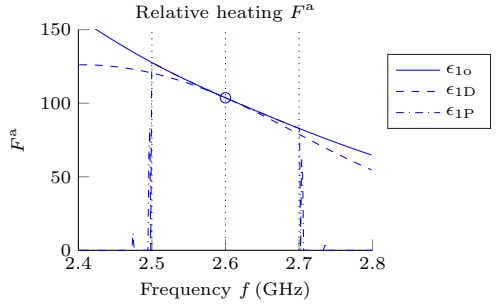

Figure 10. Relative heating F^a corresponding to the target conjugate match $\epsilon_{1\mathrm{o}}$, the tuned Drude model $\epsilon_{1\mathrm{D}}$ and the optimized passive model $\epsilon_{1\mathrm{P}}$. The surrounding medium is a saline solution with conductivity $\sigma = 1$ S/m and the approximation domain is $\Omega = [2.5, 2.7]$ GHz.

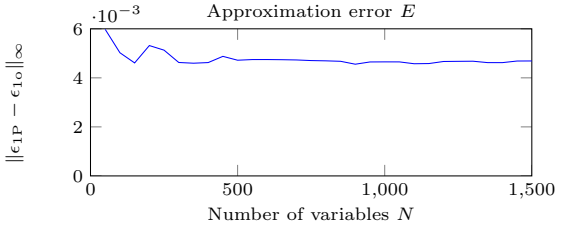

Figure 11. Approximation error $E = \|\epsilon_{1\mathrm{P}} - \epsilon_{1\mathrm{o}}\|_\infty$ as a function of the number of approximating basis functions N. The surrounding medium is a saline solution with conductivity $\sigma = 1$ S/m and the approximation domain is $\Omega = [2.5, 2.7]$ GHz. The target permittivity is the desired conjugate match $\epsilon_{1\mathrm{o}}(\omega) = -2\epsilon^*(\omega)$ for $\omega \in \Omega$.

In Figure 9 it is further noted that $\epsilon_{1\mathrm{o}}(\omega)$ is almost constant over the bandwidth of interest, and it was found that the optimized result $\epsilon_{1\mathrm{P}}(\omega)$ does not change notably if the target function is chosen according to the constant value $-156.1 + \mathrm{i}37.61 \approx \epsilon_{1\mathrm{o}}(\omega)$ for $\omega \in \Omega$. In Figure 10 is plotted the corresponding relative heating F^a according to the target conjugate match $\epsilon_{1\mathrm{o}}(\omega)$, the tuned Drude model $\epsilon_{1\mathrm{D}}(\omega)$ and the optimized model $\epsilon_{1\mathrm{P}}(\omega)$, respectively, plotted as functions of frequency between 2.4 and 2.8 GHz. Note that the optimal heating capability increases at lower frequencies and that the Drude model is tuned here to the desired center frequency $f_\mathrm{d} = 2.6$ GHz. It is seen that the optimized passive model $\epsilon_{1\mathrm{P}}(\omega)$ closely matches the heating obtained from the target conjugate match $\epsilon_{1\mathrm{o}}(\omega)$ when evaluated inside the approximation domain between 2.5 and 2.7 GHz. However, there is in fact a remaining approximation error between $\epsilon_{1\mathrm{P}}(\omega)$ and $\epsilon_{1\mathrm{o}}(\omega)$, even though it is so small that it is not visible in Figures 9 and 10. Hence, in Figure 11 is shown the approximation error $E = \sup_\Omega |\epsilon_{1\mathrm{P}}(\omega) - \epsilon_{1\mathrm{o}}(\omega)|$ plotted as a function of the number of basis functions used N. It is seen that the remaining error converges to a small non-zero value for large N.

3.4. A comment on metamaterials

When applying the conjugate match for a lossless background, the result is $\epsilon_{1\mathrm{o}} = -2\epsilon$, which is a negative real number. A material with a negative real permittivity over a specified bandwidth is sometimes regarded a *metamaterial*. In [24] is shown that a metamaterial with a constant real-valued and negative target permittivity $\epsilon_\mathrm{t} < 0$ over a finite frequency band Ω can only be approximated by a passive permittivity function $\epsilon_\mathrm{P}(\omega)$ within the following lower bound

$$\sup_{\omega\in\Omega} |\epsilon_\mathrm{P}(\omega) - \epsilon_\mathrm{t}| \geq \frac{(\epsilon_\infty - \epsilon_\mathrm{t})\frac{1}{2}B}{1 + \frac{B}{2}} = E_B, \tag{30}$$

where ϵ_∞ is the prescribed high frequency permittivity of $\epsilon_\mathrm{P}(\omega)$ and $\Omega = \omega_\mathrm{d}[1 - \frac{B}{2}, 1 + \frac{B}{2}]$ the approximation

domain, where ω_{d} is the center frequency and B the relative bandwidth with $0 < B < 2$. This physical bound has been derived solely based on the assumption of linearity, time-translational invariance and passivity by employing the theory for Herglotz functions (or equivalently the so-called Positive Real functions) and its associated sum rules [24]. It should be noted that the bound (30) is an ultimate physical bound that must be satisfied by any passive material, but it is not necessarily achievable (tight). To this end, the convex optimization approach (29) provides a complementary technique to study the realizability of such physical bounds, *cf.*, [25].

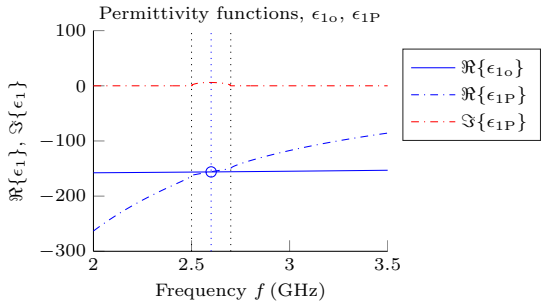

Figure 12. Permittivity functions corresponding to the conjugate match $\epsilon_{1\mathrm{o}}$, the tuned Drude model $\epsilon_{1\mathrm{D}}$ and the optimized passive model $\epsilon_{1\mathrm{P}}$. The surrounding medium is a saline solution with conductivity $\sigma = 1\,\mathrm{S/m}$ and the approximation domain is $\Omega = [2.5, 2.7]\,\mathrm{GHz}$. The constant target permittivity is $\epsilon_{\mathrm{t}} = -156.1 \approx \Re\{\epsilon_{1\mathrm{o}}(\omega)\}$ for $\omega \in \Omega$.

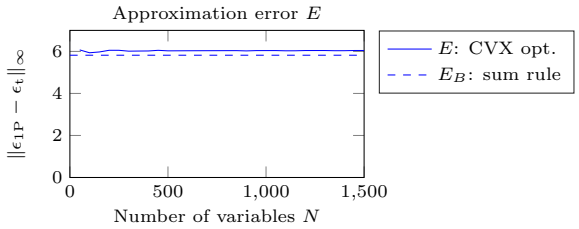

Figure 13. Approximation error $E = \|\epsilon_{1\mathrm{P}} - \epsilon_{\mathrm{t}}\|_\infty$ as a function of the number of approximating basis functions N. The surrounding medium is a saline solution with conductivity $\sigma = 1\,\mathrm{S/m}$ and the approximation domain is $\Omega = [2.5, 2.7]\,\mathrm{GHz}$. The constant target permittivity is $\epsilon_{\mathrm{t}} = -156.1 \approx \Re\{\epsilon_{1\mathrm{o}}(\omega)\}$ for $\omega \in \Omega$. Here, $B = 0.0769$ and $E_B = 5.8185$.

To illustrate the bandwidth limitation associated with such metamaterials, it is shown in Figure 12 the corresponding optimization results when the target permittivity $\epsilon_{1\mathrm{o}}(\omega)$ has been replaced for the constant real negative value $\epsilon_{\mathrm{t}} = -156.1 \approx \Re\{\epsilon_{1\mathrm{o}}(\omega)\}$ for $\omega \in \Omega$. In Figure 13 is shown the corresponding approximation error E as a function of the number of basis functions N in a comparison to the ultimate lower bound (30). It is noted that the realizable error E is only slightly larger than the ultimate physical bound E_B in (30).

The following interesting features are observed regarding the approximation of metamaterials in this particular numerical example.

- The problem to approximate the conjugate match $\epsilon_{1\mathrm{o}}$ over a finite frequency band Ω as in section 3.3 is essentially the same as to approximate a metamaterial with a constant complex value $\epsilon_{\mathrm{t}} = -156.1 + \mathrm{i}37.61 \approx \epsilon_{1\mathrm{o}}(\omega)$ for $\omega \in \Omega$. This is a situation in which the result (30) cannot be straightforwardly extended but convex optimization (29) can be used to study the realizability and the bandwidth capabilities of such a hypothetical passive material.
- Whereas the approximation of a metamaterial with a constant real negative permittivity over a finite bandwidth implies severe bandwidth limitations, the presence of an additional constant imaginary part in the target permittivity implies that the bandwidth limitation is no longer severe, and there exist a hypothetical passive (realizable) permittivity function that can approximate the metamaterial (the conjugate match) with a very small approximation error over the whole approximation domain Ω, as illustrated in Figures 9 through 11.

4. Summary

This paper presents a study on the physical limitations for radio frequency absorption in gold nanoparticle (GNP) suspensions. The analysis is based on classical electromagnetic theory regarding the energy absorption in small spherical particles in a lossy medium (*cf.*, general Mie theory) and is extended here to take the skin effect of the surrounding medium into account. The main theoretical result is the derivation of an optimal conjugate match with respect to the surrounding medium giving a physical limitation for the maximal absorption inside a spherical suspension of GNPs. As such, the theoretical result defines an optimum plasmonic resonance inside a lossy environment, and which can furthermore be put into the framework of approximating a metamaterial over a given bandwidth. The heating is quantified by a relative heating coefficient, and it is demonstrated that for a surrounding medium consisting of a weak electrolyte solution, a significant RF-heating can be achieved inside the GNP suspension, provided that an electrophoretic particle acceleration mechanism described by the Drude model is physically valid, and can be tuned into resonance at the desired frequency. The optimally tuned Drude model can furthermore be used as a benchmark in a comparison based on realistic parameter choices regarding the volume fraction, mass, charge, and friction constant of the GNPs. The most uncertain parameter that seems to be difficult

to model, measure and control is the charge number of the coated gold nanoparticles. Interestingly enough, our study shows that this parameter is also one of the most sensitive and important when determining the achievable heating.

Acknowledgments

This work was supported by the Swedish Foundation for Strategic Research (SSF).

Appendix A. Vector spherical waves

The definition of the vector spherical waves together with some important results that are not readily available in the literature are presented in this appendix. In particular, we supply explicit formulas for the transition matrices $t_{\tau l}$ and $r_{\tau l}$ defined in (A.8) and (A.9) below, as well as the energies (as squared integrals) of the spherical Bessel functions (A.15) and the regular vector waves (A.20) and (A.21) in the case with lossy materials. The squared integrals are based on the first Lommel integral in the case when the wavenumber k is complex valued.

Appendix A.1. Definition of vector spherical waves

In a source-free region the electromagnetic field can be expanded in vector spherical waves as

$$\boldsymbol{E}(\boldsymbol{r}) = \sum_{l,m,\tau} a_{\tau ml}\mathbf{v}_{\tau ml}(k\boldsymbol{r}) + b_{\tau ml}\mathbf{u}_{\tau ml}(k\boldsymbol{r}), \tag{A.1}$$

$$\boldsymbol{H}(\boldsymbol{r}) = \frac{1}{\mathrm{i}\eta_0\eta}\sum_{l,m,\tau} a_{\tau ml}\mathbf{v}_{\bar{\tau} ml}(k\boldsymbol{r}) + b_{\tau ml}\mathbf{u}_{\bar{\tau} ml}(k\boldsymbol{r}),$$

where $\mathbf{v}_{\tau ml}(k\boldsymbol{r})$ and $\mathbf{u}_{\tau ml}(k\boldsymbol{r})$ are the regular and the outgoing vector spherical waves, respectively, and $a_{\tau ml}$ and $b_{\tau ml}$ the corresponding multipole coefficients, see *e.g.*, [18, 33–35]. Here, $l = 1, \ldots, \infty$, $m = -l, \ldots, l$ and $\tau = 1, 2$, where $\tau = 1$ indicates a transverse electric (TE) magnetic multipole and $\tau = 2$ a transverse magnetic (TM) electric multipole, and $\bar{\tau}$ denotes the complement of τ, *i.e.*, $\bar{1} = 2$ and $\bar{2} = 1$.

The solenoidal (source-free) regular vector spherical waves are defined here by

$$\begin{aligned}\mathbf{v}_{1ml}(k\boldsymbol{r}) &= \frac{1}{\sqrt{l(l+1)}}\nabla\times(\boldsymbol{r}\mathrm{j}_l(kr)\mathrm{Y}_{ml}(\hat{\boldsymbol{r}})) \\ &= \mathrm{j}_l(kr)\mathbf{A}_{1ml}(\hat{\boldsymbol{r}}),\end{aligned} \tag{A.2}$$

$$\begin{aligned}\mathbf{v}_{2ml}(k\boldsymbol{r}) &= \frac{1}{k}\nabla\times\mathbf{v}_{1ml}(k\boldsymbol{r}) \\ &= \frac{(kr\mathrm{j}_l(kr))'}{kr}\mathbf{A}_{2ml}(\hat{\boldsymbol{r}}) + \sqrt{l(l+1)}\frac{\mathrm{j}_l(kr)}{kr}\mathbf{A}_{3ml}(\hat{\boldsymbol{r}}),\end{aligned} \tag{A.3}$$

where $\mathrm{Y}_{ml}(\hat{\boldsymbol{r}})$ are the spherical harmonics, $\mathbf{A}_{\tau ml}(\hat{\boldsymbol{r}})$ the vector spherical harmonics and $\mathrm{j}_l(x)$ the spherical Bessel functions of order l, *cf.*, [18, 19, 33–35]. Here, $(\cdot)'$ denotes a differentiation with respect to the argument of the spherical Bessel function. The outgoing (radiating) vector spherical waves $\mathbf{u}_{\tau ml}(k\boldsymbol{r})$ are obtained by replacing the regular spherical Bessel functions $\mathrm{j}_l(x)$ above for the spherical Hankel functions of the first kind, $\mathrm{h}_l^{(1)}(x)$, see [18, 19, 33].

The vector spherical harmonics $\mathbf{A}_{\upsilon lm}(\hat{\boldsymbol{r}})$ are given by

$$\mathbf{A}_{1ml}(\hat{\boldsymbol{r}}) = \frac{1}{\sqrt{l(l+1)}}\nabla\times(\boldsymbol{r}\mathrm{Y}_{ml}(\hat{\boldsymbol{r}})), \tag{A.4}$$

$$\mathbf{A}_{2ml}(\hat{\boldsymbol{r}}) = \hat{\boldsymbol{r}}\times\mathbf{A}_{1ml}(\hat{\boldsymbol{r}}), \tag{A.5}$$

$$\mathbf{A}_{3ml}(\hat{\boldsymbol{r}}) = \hat{\boldsymbol{r}}\mathrm{Y}_{ml}(\hat{\boldsymbol{r}}), \tag{A.6}$$

where $\upsilon = 1, 2, 3$, and where the spherical harmonics $\mathrm{Y}_{ml}(\hat{\boldsymbol{r}})$ are given by

$$\mathrm{Y}_{ml}(\hat{\boldsymbol{r}}) = (-1)^m\sqrt{\frac{2l+1}{4\pi}}\sqrt{\frac{(l-m)!}{(l+m)!}}\mathrm{P}_l^m(\cos\theta)\mathrm{e}^{\mathrm{i}m\phi},$$

and where $\mathrm{P}_l^m(x)$ are the associated Legendre functions [18, 19, 34]. The vector spherical harmonics are orthonormal on the unit sphere, and hence

$$\int_{\Omega_0}\mathbf{A}^*_{\upsilon ml}(\hat{\boldsymbol{r}})\cdot\mathbf{A}_{\upsilon' m' l'}(\hat{\boldsymbol{r}})\mathrm{d}\Omega = \delta_{\upsilon\upsilon'}\delta_{mm'}\delta_{ll'}, \tag{A.7}$$

where Ω_0 denotes the unit sphere and $\mathrm{d}\Omega = \sin\theta\mathrm{d}\theta\mathrm{d}\phi$.

Appendix A.2. Transition matrices for a homogeneous sphere

Consider the scattering of an electromagnetic field due to a homogeneous sphere of radius r_1, permittivity ϵ_1, permeability μ_1 and wavenumber $k_1 = k_0\sqrt{\mu_1\epsilon_1}$. The medium surrounding the sphere is characterized by the permittivity ϵ, permeability μ and wave number $k = k_0\sqrt{\mu\epsilon}$. The incident and the scattered fields for $r > r_1$ are expressed as in (A.1) with multipole coefficients $a_{\tau ml}$ and $b_{\tau ml}$, respectively, and the interior field is similarly expressed using regular vector spherical waves for $r < r_1$ with multipole coefficients $a^{(1)}_{\tau ml}$. By matching the tangential electric and magnetic fields at the boundary of radius r_1, it can be shown that

$$b_{\tau ml} = t_{\tau l}a_{\tau ml}, \tag{A.8}$$

$$a^{(1)}_{\tau ml} = r_{\tau l}a_{\tau ml}, \tag{A.9}$$

where $t_{\tau l}$ and $r_{\tau l}$ are transition matrices for scattering and absorption given by

$$t_{1l} = \frac{\mathrm{j}_l(kr_1)(k_1r_1\mathrm{j}_l(k_1r_1))'\mu - \mathrm{j}_l(k_1r_1)(kr_1\mathrm{j}_l(kr_1))'\mu_1}{\mathrm{j}_l(k_1r_1)(kr_1\mathrm{h}_l^{(1)}(kr_1))'\mu_1 - \mathrm{h}_l^{(1)}(kr_1)(k_1r_1\mathrm{j}_l(k_1r_1))'\mu},$$

$$t_{2l} = \frac{\mathrm{j}_l(k_1r_1)(kr_1\mathrm{j}_l(kr_1))'\epsilon_1 - \mathrm{j}_l(kr_1)(k_1r_1\mathrm{j}_l(k_1r_1))'\epsilon}{\mathrm{h}_l^{(1)}(kr_1)(k_1r_1\mathrm{j}_l(k_1r_1))'\epsilon - \mathrm{j}_l(k_1r_1)(kr_1\mathrm{h}_l^{(1)}(kr_1))'\epsilon_1},$$

$$r_{1l} = \frac{\mathrm{j}_l(kr_1)(kr_1\mathrm{h}_l^{(1)}(kr_1))'\mu_1 - \mathrm{h}_l^{(1)}(kr_1)(kr_1\mathrm{j}_l(kr_1))'\mu_1}{\mathrm{j}_l(k_1r_1)(kr_1\mathrm{h}_l^{(1)}(kr_1))'\mu_1 - \mathrm{h}_l^{(1)}(kr_1)(k_1r_1\mathrm{j}_l(k_1r_1))'\mu},$$

$$r_{2l} = -\frac{(\mathrm{j}_l(kr_1)(kr_1\mathrm{h}_l^{(1)}(kr_1))' - \mathrm{h}_l^{(1)}(kr_1)(kr_1\mathrm{j}_l(kr_1))')\sqrt{\epsilon}\sqrt{\epsilon_1}\sqrt{\mu_1}}{(\mathrm{h}_l^{(1)}(kr_1)(k_1r_1\mathrm{j}_l(k_1r_1))'\epsilon - \mathrm{j}_l(k_1r_1)(kr_1\mathrm{h}_l^{(1)}(kr_1))'\epsilon_1)\sqrt{\mu}}.$$

Appendix A.3. First Lommel integral for spherical Bessel functions with complex-valued argument

The first Lommel integral is given by

$$\int \mathrm{C}_\nu(a\rho)\mathrm{D}_\nu(b\rho)\rho\mathrm{d}\rho \tag{A.10}$$
$$= \frac{\rho\left(a\mathrm{C}_{\nu+1}(a\rho)\mathrm{D}_\nu(b\rho) - b\mathrm{C}_\nu(a\rho)\mathrm{D}_{\nu+1}(b\rho)\right)}{a^2-b^2},$$

where a and b are complex-valued constants and $\mathrm{C}_\nu(\cdot)$ and $\mathrm{D}_\nu(\cdot)$ are arbitrary cylinder functions, *i.e.*, the Bessel function, the Neumann function, the Hankel functions of the first and second kind $\mathrm{J}_\nu(\cdot)$, $\mathrm{Y}_\nu(\cdot)$, $\mathrm{H}_\nu^{(1)}(\cdot)$, $\mathrm{H}_\nu^{(2)}(\cdot)$, respectively, or any nontrivial linear combination of these functions, see 10.22.4 and 10.22.5 in [19], and pp. 133–134 in [36].

Let $a=\kappa$ and $b=\kappa^*$, where $\kappa\neq\kappa^*$, *i.e.*, κ is not real valued, and consider the case

$$\mathrm{C}_\nu(\kappa\rho) = A\mathrm{J}_\nu(\kappa\rho) + B\mathrm{H}_\nu^{(1)}(\kappa\rho), \tag{A.11}$$

where A and B are complex-valued constants. Let

$$\mathrm{D}_\nu(\kappa^*\rho) = \mathrm{C}_\nu^*(\kappa\rho) = A^*\mathrm{J}_\nu(\kappa^*\rho) + B^*\mathrm{H}_\nu^{(2)}(\kappa^*\rho), \tag{A.12}$$

where the conjugate rules $\mathrm{J}_\nu^*(\zeta) = \mathrm{J}_\nu(\zeta^*)$ and $\mathrm{H}_\nu^{(1)^*}(\zeta) = \mathrm{H}_\nu^{(2)}(\zeta^*)$ have been used, *cf.*, [19]. The first Lommel integral (A.10) now yields

$$\int |\mathrm{C}_\nu(\kappa\rho)|^2\rho\mathrm{d}\rho = \frac{\rho\Im\{\kappa\mathrm{C}_{\nu+1}(\kappa\rho)\mathrm{C}_\nu^*(\kappa\rho)\}}{\Im\{\kappa^2\}}. \tag{A.13}$$

The spherical Bessel, Neumann and Hankel functions of the first and second kind are given by $\mathrm{j}_l(\zeta) = \sqrt{\frac{\pi}{2\zeta}}\mathrm{J}_{l+1/2}(\zeta)$, $\mathrm{y}_l(\zeta) = \sqrt{\frac{\pi}{2\zeta}}\mathrm{Y}_{l+1/2}(\zeta)$, $\mathrm{h}_l^{(1)}(\zeta) = \sqrt{\frac{\pi}{2\zeta}}\mathrm{H}_{l+1/2}^{(1)}(\zeta)$ and $\mathrm{h}_l^{(2)}(\zeta) = \sqrt{\frac{\pi}{2\zeta}}\mathrm{H}_{l+1/2}^{(2)}(\zeta)$, respectively, *cf.*, [19]. An arbitrary linear combination of spherical Bessel and Hankel functions can hence be written as

$$\mathrm{s}_l(kr) = A\mathrm{j}_l(kr) + B\mathrm{h}_l^{(1)}(kr) = \sqrt{\frac{\pi}{2kr}}\mathrm{C}_{l+1/2}(kr), \tag{A.14}$$

where $\mathrm{C}_{l+1/2}(kr)$ is the corresponding cylinder function as defined in (A.11). The first Lommel integral for spherical Bessel functions with complex-valued arguments can now be derived as

$$\int |\mathrm{s}_l(kr)|^2 r^2\mathrm{d}r = \frac{\pi}{2|k|}\int \left|\mathrm{C}_{l+1/2}(kr)\right|^2 r\mathrm{d}r \tag{A.15}$$
$$= \frac{\pi}{2|k|}\frac{r\Im\left\{k\mathrm{C}_{l+1+1/2}(kr)\mathrm{C}_{l+1/2}^*(kr)\right\}}{\Im\{k^2\}}$$
$$= \frac{r^2\Im\left\{k\sqrt{\frac{\pi}{2kr}}\mathrm{C}_{l+1+1/2}(kr)\left(\sqrt{\frac{\pi}{2kr}}\mathrm{C}_{l+1/2}(kr)\right)^*\right\}}{\Im\{k^2\}}$$
$$= \frac{r^2\Im\{k\mathrm{s}_{l+1}(kr)\mathrm{s}_l^*(kr)\}}{\Im\{k^2\}}.$$

Appendix A.4. Orthogonality of the regular spherical waves

Due to the orthonormality of the vector spherical harmonics (A.7), the regular spherical waves are orthogonal over the unit sphere with

$$\int_{\Omega_0} \mathbf{v}_{\tau ml}^*(k\boldsymbol{r})\cdot\mathbf{v}_{\tau'm'l'}(k\boldsymbol{r})\mathrm{d}\Omega \tag{A.16}$$
$$= \delta_{\tau\tau'}\delta_{mm'}\delta_{ll'}S_{\tau l}(k,r),$$

where

$$S_{\tau l}(k,r) = \int_{\Omega_0}|\mathbf{v}_{\tau ml}(k\boldsymbol{r})|^2\mathrm{d}\Omega \tag{A.17}$$
$$= \begin{cases} |\mathrm{j}_l(kr)|^2 & \text{for } \tau=1,\\ \left|\frac{\mathrm{j}_l(kr)}{kr}+\mathrm{j}_l'(kr)\right|^2 + l(l+1)\left|\frac{\mathrm{j}_l(kr)}{kr}\right|^2 & \text{for } \tau=2.\end{cases}$$

As a consequence, the regular spherical waves are also orthogonal over a spherical volume V_{r_1} with radius r_1 yielding

$$\int_{V_{r_1}} \mathbf{v}_{\tau ml}^*(k\boldsymbol{r})\cdot\mathbf{v}_{\tau'm'l'}(k\boldsymbol{r})\mathrm{d}v \tag{A.18}$$
$$= \delta_{\tau\tau'}\delta_{mm'}\delta_{ll'}W_{\tau l}(k,r_1),$$

where

$$W_{\tau l}(k,r_1) = \int_{V_{r_1}}|\mathbf{v}_{\tau ml}(k\boldsymbol{r})|^2\,\mathrm{d}v \tag{A.19}$$
$$= \int_0^{r_1} S_{\tau l}(k,r)r^2\mathrm{d}r,$$

where $\mathrm{d}v = r^2\mathrm{d}\Omega\mathrm{d}r$ and $\tau=1,2$.

For complex-valued arguments k, $W_{1l}(k,r_1)$ is obtained from (A.15) as

$$W_{1l}(k,r_1) = \int_0^{r_1}|\mathrm{j}_l(kr)|^2\,r^2\mathrm{d}r \tag{A.20}$$
$$= \frac{r_1^2\Im\{k\mathrm{j}_{l+1}(kr_1)\mathrm{j}_l^*(kr_1)\}}{\Im\{k^2\}}.$$

By using the following recursive relationships

$$\frac{\mathrm{j}_l(kr)}{kr} = \frac{1}{2l+1}\left(\mathrm{j}_{l-1}(kr)+\mathrm{j}_{l+1}(kr)\right),$$
$$\mathrm{j}_l'(kr) = \frac{1}{2l+1}\left(l\mathrm{j}_{l-1}(kr) - (l+1)\mathrm{j}_{l+1}(kr)\right),$$

where $l=1,2,\ldots$, *cf.*, [19], it can be shown that

$$W_{2l}(k,r_1) \tag{A.21}$$
$$= \int_0^{r_1}\left(\left|\frac{\mathrm{j}_l(kr)}{kr}+\mathrm{j}_l'(kr)\right|^2 + l(l+1)\left|\frac{\mathrm{j}_l(kr)}{kr}\right|^2\right)r^2\mathrm{d}r$$
$$= \frac{1}{2l+1}\left((l+1)W_{1,l-1}(k,r_1) + lW_{1,l+1}(k,r_1)\right).$$

References

[1] C. B. Collins, R. S. McCoy, B. J. Ackerson, G. J. Collins, and C. J. Ackerson. Radiofrequency heating pathways for gold nanoparticles. *Nanoscale*, 6:8459–8472, 2014.

[2] E. Sassaroli, K. C. P. Li, and B. E. O'Neil. Radio frequency absorption in gold nanoparticle suspensions: a phenomenological study. *J. Phys. D: Appl. Phys.*, 45:1–15, 2012. 075303.

[3] J. Cardinal, J. R. Klune, E. Chory, G. Jeyabalan, J. S. Kanzius, M. Nalesnik, and D. A. Geller. Noninvasive radiofrequency ablation of cancer targeted by gold nanoparticles. *Surgery*, 144(2):125–132, 2008.

[4] C. J. Gannon, C. R. Patra, R. Bhattacharya, P. Mukherjee, and S. A Curley. Intracellular gold nanoparticles enhance non-invasive radiofrequency thermal destruction of human gastrointestinal cancer cells. *Journal of Nanobiotechnology*, 6(2):1–9, 2008.

[5] C. H. Moran, S. M. Wainerdi, T. K. Cherukuri, C. Kittrell, B. J. Wiley, N. W. Nicholas, S. A. Curley, J. S. Kanzius, and P. Cherukuri. Size-dependent joule heating of gold nanoparticles using capacitively coupled radiofrequency fields. *Nano Res*, 2:400–405, 2009.

[6] M.A.M. Marquez, E.G. Garcia, and M.A.F. Camacho. Hyperthermia devices and their uses with nanoparticles, June 11 2013. US Patent 8463397, https://www.google.com/patents/US8463397.

[7] G. L. DeNardo and S. J. DeNardo. Turning the heat on cancer. *Cancer Biotherapy & Radiopharmaceuticals*, 23(6):671–679, 2008.

[8] M. F. Callaghan, T. Lund, P. Hashemzadeh, I. M. Roitt, and R. H. Bayford. An investigation of the impedance properties of gold. In *Journal of Physics: Conference Series*, volume 224, pages 1–4. International Conference on Electrical Bioimpedance, 2010. 012058.

[9] E. C. Dreaden, A. M. Alkilany, X. Huang, C. J. Murphy, and M. A. El-Sayed. The golden age: gold nanoparticles for biomedicine. *Chem. Soc. Rev.*, 41:2740–2779, 2012.

[10] B. Hildebrandt, P. Wust, O. Ahlers, A. Dieing, G. Sreenivasa, T. Kerner, R. Felix, and H. Riess. The cellular and molecular basis of hyperthermia. *Critical Reviews in Oncology/Hematology*, 43(1):33–56, 2002.

[11] S. J. Corr, M. Raoof, Y. Mackeyev, S. Phounsavath, M. A. Cheney, B. T. Cisneros, M. Shur, M. Gozin, P. J. McNally, L. J. Wilson, and S. A. Curley. Citrate-capped gold nanoparticle electrophoretic heat production in response to a time-varying radio-frequency electric field. *J. Phys. Chem. C*, 116(45):24380–24389, 2012.

[12] A. Gupta, R. S. Kane, and D-A. Borca-Tasciuc. Local temperature measurement in the vicinity of electromagnetically heated magnetite and gold nanoparticles. *J. Appl. Phys.*, 108, 2010. 064901.

[13] X. Liu, H j. Chen, X. Chen, C. Parinia, and D. Wen. Low frequency heating of gold nanoparticle dispersions for non-invasive thermal therapies. *Nanoscale*, 4:3945–3953, 2012.

[14] D. Li, Y. S. Jung, S. Tan, H. K. Kim, E. Chory, and D. A. Geller. Negligible absorption of radiofrequency radiation by colloidal gold nanoparticles. *Journal of Colloid and Interface Science*, 358:47–53, 2011.

[15] G. W. Hanson, R. C. Monreal, and S. P. Apell. Electromagnetic absorption mechanisms in metal nanospheres: bulk and surface effects in radiofrequency-terahertz heating of nanoparticles. *J. Appl. Phys.*, 109, 2011. 124306.

[16] O. D. Miller, A. G. Polimeridis, M. T. H. Reid, C. W. Hsu, B. G. DeLacy, J. D. Joannopoulos, M. Soljacic, and S. G. Johnson. Fundamental limits to optical response in absorptive systems. *Optics Express*, 24(4):3329–3364, 2016.

[17] M. N. Martin, J. I. Basham, P. Chando, and S-K Eah. Charged gold nanoparticles in non-polar solvents: 10-min synthesis and 2D self-assembly. *Langmuir*, 2010.

[18] J. D. Jackson. *Classical Electrodynamics*. John Wiley & Sons, New York, third edition, 1999.

[19] F. W. J. Olver, D. W. Lozier, R. F. Boisvert, and C. W. Clark. *NIST Handbook of mathematical functions*. Cambridge University Press, New York, 2010.

[20] Robert E. Greene and Steven G. Krantz. *Function theory of one complex variable*. John Wiley & Sons, New York, 1997.

[21] C. F. Bohren and D. R. Huffman. *Absorption and Scattering of Light by Small Particles*. John Wiley & Sons, New York, 1983.

[22] C. F. Bohren and D. P. Gilra. Extinction by a spherical particle in an absorbing medium. *J. Colloid Interface Sci.*, 72(2):215–221, 1979.

[23] P. Chylek. Light scattering by small particles in an absorbing medium. *J. Opt. Soc. Am.*, 67(4):561–563, 1977.

[24] M. Gustafsson and D. Sjöberg. Sum rules and physical bounds on passive metamaterials. *New Journal of Physics*, 12:043046, 2010.

[25] S. Nordebo, M. Gustafsson, B. Nilsson, and D. Sjöberg. Optimal realizations of passive structures. *IEEE Trans. Antennas Propagat.*, 62(9):4686–4694, 2014.

[26] A. H. Zemanian. *Distribution theory and transform analysis: an introduction to generalized functions, with applications*. McGraw-Hill, New York, 1965.

[27] I. S. Kac and M. G. Krein. R-functions - Analytic functions mapping the upper halfplane into itself. *Am. Math. Soc. Transl.*, 103(2):1–18, 1974.

[28] N. I. Akhiezer. *The classical moment problem*. Oliver and Boyd, 1965.

[29] H. M. Nussenzveig. *Causality and dispersion relations*. Academic Press, London, 1972.

[30] Anders Bernland, Annemarie Luger, and Mats Gustafsson. Sum rules and constraints on passive systems. *Journal of Physics A: Mathematical and Theoretical*, 44(14):145205–, 2011.

[31] F. W. King. *Hilbert transforms vol. I–II*. Cambridge University Press, 2009.

[32] M. Grant and S. Boyd. CVX: A system for disciplined convex programming, release 2.0, ©2012 CVX Research, Inc., Austin, TX.

[33] A. Boström, G. Kristensson, and S. Ström. Transformation properties of plane, spherical and cylindrical scalar and vector wave functions. In V. V. Varadan, A. Lakhtakia, and V. K. Varadan, editors, *Field Representations and Introduction to Scattering*, Acoustic, Electromagnetic and Elastic Wave Scattering, chapter 4, pages 165–210. Elsevier Science Publishers, Amsterdam, 1991.

[34] George B. Arfken and Hans J. Weber. *Mathematical Methods for Physicists*. Academic Press, New York, fifth edition, 2001.

[35] Roger G. Newton. *Scattering Theory of Waves and Particles*. Dover Publications, New York, second edition, 2002.

[36] G. N. Watson. *A Treatise on the Theory of Bessel Functions*. Cambridge University Press, Cambridge, U.K., second edition, 1995.